

Measuring the Slope of the Dust Extinction Law and the Power Spectrum of Dust Clouds Using Differentially-Reddened Globular Clusters

J. Melbourne and P. Guhathakurta

UCO/Lick Observatory, Department of Astronomy and Astrophysics, University of California at Santa Cruz, 1156 High Street, Santa Cruz, California 95064

jmel, raja@ucolick.org

ABSTRACT

We present three methods for measuring the slope of the Galactic dust extinction law, R_V , and a method for measuring the fine-scale structure of dust clouds in the direction of differentially-reddened globular clusters. We apply these techniques to *BVI* photometry of stars in the low-latitude Galactic globular cluster NGC 4833 which displays spatially-variable extinction/reddening about a mean $\langle A_V \rangle \approx 1$. An extensive suite of Monte Carlo simulations is used to characterize the efficacy of the methods. The essence of the first two methods is to determine, for an assumed value of R_V , the *relative* visual extinction δA_V of each cluster horizontal branch (HB) star with respect to an empirical HB locus; the locus is derived from the color-magnitude diagram (CMD) of a subset of stars in a small region near the cluster center for which differential extinction/reddening are relatively small. A star-by-star comparison of δA_V from the $(B - V, V)$ CMD with that from the $(V - I, V)$ CMD is used to find the optimal R_V . In the third method, R_V is determined by minimizing the scatter in the HB in the $(B - V, V)$ CMD after correcting the photometry for extinction and reddening using the Schlegel, Finkbeiner, & Davis (1998) dust maps. The weighted average of the results from the three methods gives $R_V = 3.0 \pm 0.4$ for the dust along the line of sight to NGC 4833. The fine-scale structure of the dust is quantified via the difference, $(\Delta A_V)_{ij} \equiv (\delta A_V)_i - (\delta A_V)_j$, between pairs of cluster HB stars (i, j) as a function of their angular separation r_{ij} . The variance (mean square scatter) of $(\Delta A_V)_{ij}$ is found to have a power-law dependence on angular scale: $\text{var}(r) \propto r^\beta$, with $\beta = +0.9 \pm 0.1$. This translates into an angular power spectrum $P(\kappa) \propto \kappa^\alpha$, with the index $\alpha = -1.9 \pm 0.1$ for $r \sim 1'-5'$, where $\kappa \equiv 1/r$. The dust angular power spectrum on small scales (from optical data) matches smoothly onto the larger-scale power spectrum derived from Schlegel et al.'s far-infrared map of the dust thermal emission.

Subject headings: Galaxy: globular clusters: individual NGC 4833 — ISM: dust, extinction — ISM: structure

1. Introduction

Scattering, absorption, and reradiation of photons by dust grains affect the propagation of starlight and play a key role in regulating the energy balance in the interstellar medium. Studies of these processes have provided a great deal of insight into the physical and chemical properties of dust grains (for reviews of dust properties, see Mathis 1990a; Witt 2003). It is also important to disentangle the effects of intervening dust from many kinds of astronomical observations, ranging from photometry and spectroscopy of Galactic stars and external galaxies to mapping small-scale anisotropy in the Cosmic Microwave Background Radiation (CMBR).

1.1. Reddening Law and Dust Grain Properties

The degree of absorption and scattering by dust depends, in general, on the wavelength of the incident radiation (Whitford 1958). This dependence can be quantified in terms of the normalized dust extinction law A_λ/A_V (or reddening law), where extinction is the sum of absorption plus scattering. The ratio of total to selective extinction, $R_V \equiv A_V/E(B - V)$, is a commonly-used measure of the slope of the extinction/reddening law. Using data along many different Galactic sight-lines, Cardelli, Clayton, & Mathis (1989, hereafter CCM) found a tight correlation between the overall shape of the reddening law and the slope R_V . CCM devised an R_V -based, one-parameter family of empirical fitting functions to characterize the observed range of extinction law shapes; this parameterization was later refined by Fitzpatrick (1999).

Galactic dust displays a wide range of behavior. While diffuse interstellar dust is observed to have $R_V = 3.1$ *on average* (Savage & Mathis 1979; CCM), this value is by no means universal. Significant deviations from this canonical $R_V = 3.1$ value (and corresponding differences in the overall shape of the extinction/reddening law) are known to exist for a variety of interstellar dust clouds, and these variations appear to be generally correlated with environment (Fitzpatrick 1999). For example, R_V has been found to range from 4 to 5 in dense molecular clouds (Mathis 1990b; Larson, Whittet, & Hough 1996; Whittet et al. 2001), whereas there are indications that more diffuse, high-latitude cirrus clouds may have R_V values as small as ~ 2 (Fitzpatrick & Massa 1990; Larson et al. 1996; Szomoru & Guhathakurta 1999). Studies based on stellar photometry from the Optical Gravitational Lens Experiment (OGLE) and MAssive Compact Halo Objects (MACHO) projects point to R_V being substantially smaller than 3 in the direction of the Galactic bulge (Popowski 2000; Popowski, Cook, & Becker 2003; Udalski 2003; Sumi 2004; Popowski 2004). Barbaro et al. (2001) find departures from the CCM parameterization in the ultraviolet portion of the Galactic extinction law. It is worth noting that the above studies sample dust at a wide range of distances from the Sun: some probe the diffuse interstellar medium in its immediate vicinity whereas others, especially those at low Galactic latitudes, can probe dust at much larger distances well outside the Solar neighborhood (e.g., the RCrA cloud studied by Szomoru & Guhathakurta 1999).

Some studies have suggested that R_V variations are tied to variations in the size distribution of dust grains from one line of sight to another. In diffuse cirrus clouds, a relative abundance of small grains might explain the steep rise of the extinction curve into the ultraviolet (CCM; Larson et al. 1996). By contrast, a high abundance of large grains, which grow readily by coagulation in dense molecular clouds, may explain the larger than average values of R_V observed in these regions (Whittet et al. 2001). Whittet et al. suggest that, in dense molecular clouds, R_V remains close to the standard value of 3.1 except for lines of sight with unusually high extinction ($A_V \geq 3$). This may indicate a more complicated relationship between R_V and A_V . Moreover, it has been argued that chemical composition can also play a role in determining the shape of the extinction law (Rhoads, Malhotra, & Kochanski 2004).

To improve our understanding of the dependence of R_V on environment, measurements are necessary along many sight-lines through a broad range of cloud types. Clusters with differential extinction/reddening have long been used to measure the R_V of intervening dust (Mihalas & Routly 1968). The traditional method of spectral typing individual cluster stars (e.g., on the Morgan-Keenan system), in conjunction with photometric measurements, allows for a direct and precise measurement of extinction and reddening. However, this method of measuring R_V requires high-quality, flux-calibrated spectra and a good understanding of the effects of metallicity on the energy output of stars. Our study focuses instead on the use of broad-band photometry in light of the fact that an extensive suite of photometric data sets is currently available.

In this paper, we propose three methods for measuring the R_V of dust in the foreground of differentially-reddened globular clusters. The first two methods are closely related to each other and rely on accurate three-band optical photometry of cluster stars. The third relies on two-band optical photometry and a map of the dust thermal emission (Schlegel, Finkbeiner, & Davis 1998, hereafter SFD) and is particularly well suited to wide-field data. All three methods are based on the premise that the width of the blue horizontal branch (HB) is minimized when the appropriate R_V value is used to correct the photometry for extinction and reddening. The methods are applied to NGC 4833, a low-latitude Galactic globular cluster with variable extinction across its face. Realistic Monte Carlo simulations of the cluster data set are used to estimate the accuracy with which R_V can be recovered.

1.2. “Cirrus”—The Rich Texture of Interstellar Dust

Nearly two decades ago, Low et al. (1984) noticed diffuse background emission in the InfraRed Astronomical Satellite (IRAS) 60 and 100 μm maps and termed it ‘infrared cirrus’ due to its complex texture. The cirrus has been associated with thermal emission from dust grains in the diffuse interstellar medium (Beichman 1987). Combining the angular resolution of the IRAS observations with the photometric accuracy of the COsmic Background Explorer (COBE)/Diffuse InfraRed Background Experiment (DIRBE) data, SFD derived all-sky maps of the dust column density and mean temperature. One of the primary uses of these maps has been to correct extragalactic sources

for extinction and reddening.

The SFD maps show structure in the cirrus down to the smallest angular scales resolved by IRAS ($\approx 6'$). Gautier et al. (1992) described the structure in the IRAS data in terms of its angular power spectrum,

$$P(\kappa) \propto \kappa^\alpha \quad , \quad (1)$$

where P is the Fourier power, κ is the reciprocal of the angular scale, and $\alpha \sim -3$ is the spectral index. Similarly, Guhathakurta & Cutri (1994) examined both IRAS $100\ \mu\text{m}$ maps and optical CCD surface photometry of reprocessed starlight from dust grains: they found that power on small scales was dominated by stars and galaxies, and since it was impossible to completely separate out these components, they merely cleared out the obvious compact “objects” (stars and galaxies) and smoothed the residual image over arcminute scales; the resulting power spectrum had an index $\alpha = -3$. More recently, Kiss et al. (2003) observed 13 fields with Infrared Space Observatory (ISO)/ISOPHOT and found that the power spectrum index varies from field to field over the range $-5.3 \leq \alpha \leq -2.1$ for angular scales larger than $3'$. This work extends the finding of $-3.6 \leq \alpha \leq -0.5$ by Herbstmeier et al. (1998) in their earlier ISOPHOT-based study. These last two studies indicate that $\alpha \sim -3.0$ is not universal.

In this study, the scatter in the HB of the differentially-reddened globular cluster NGC 4833 is used to measure the angular power spectrum of dust on scales smaller than the angular resolution of the thermal emission maps (e.g., IRAS, DIRBE, ISOPHOT). For uncrowded data such as ours, the smallest angular scale down to which this method can be applied is set by the surface density of HB tracers which in turn determines the typical nearest-neighbor separation; in crowding-limited situations, the smallest angular scale is a few times the size of the stellar point spread function: few arcseconds for ground-based images and sub-arcsecond for *Hubble Space Telescope* images.

Because interstellar dust causes extinction and reddening of starlight and reprocesses the energy, dust patchiness has a profound impact on the accuracy of many astronomical measurements even at high Galactic latitudes. Thermal emission from cold dust can confuse CMBR anisotropy measurements. Measurements of large-scale structure in galaxy surveys may be influenced by spatial non-uniformities in the foreground dust. Studies of stellar populations are at risk because measurements of T_{eff} can be impacted by reddening. Extinction can affect the photometry of distance indicators and thereby produce systematic errors in the distance-scale ladder. It is therefore important to quantify extinction/reddening variations on the smallest scales possible. While the SFD study does an excellent job of characterizing moderate- to large-scale dust variations, their maps miss power on scales smaller than a few arcminutes.

The photometry of NGC 4833 is presented in § 2. The construction of simulated cluster data sets is discussed in § 3. The R_V measurement methods are outlined in § 4, along with their application to NGC 4833 and simulated data sets to estimate the accuracy of each method. In § 5,

we describe the angular power spectrum of cirrus in the direction of NGC 4833. Possible future extensions of this work are discussed in § 6. The main conclusions of this paper are summarized in § 7.

2. The Data

The globular cluster NGC 4833 is located near the equatorial plane of our Galaxy ($l = 304^\circ$, $b = -8^\circ$) in a dusty region of the constellation Musca. The cluster has a mean reddening of $\langle E(B - V) \rangle = 0.32$ mag and reddening variations of order ± 0.05 mag across the field (Melbourne et al. 2000). Figure 1 of Melbourne et al. shows an image of the dusty features in the region around the cluster including the Coalsack nebula.

2.1. Multiband CCD Photometry

The Johnson-Cousins BVI stellar photometry of NGC 4833 used in this study are drawn from Melbourne et al. (2000). A detailed description of the data set is given in that paper so only a brief discussion appears here. The CCD images of the cluster were obtained in 1996 using the 0.9-m telescope at the Cerro Tololo Inter-American Observatory¹. The data reduction was carried out with the DAOPHOT II (Stetson 1994) stellar photometry package.

Figure 1 shows the $(B - V, V)$ and $(V - I, V)$ CMDs (left and right panels, respectively) for the full $13.5' \times 13.5'$ field. Boxes are drawn in the former CMD around the 260 objects that are considered to be candidate cluster HB stars for the purposes of this study (possible non-HB interlopers in the sample are discussed in § 4.1.1). Extinction/reddening variations across the field affect the width of the principal sequences of the CMDs. Figure 2 shows that the HB is relatively tight and narrow for the central $r < 2'$ region of the cluster, but increases in width for stars distributed over a larger area in the outer region of the cluster. This suggests that extinction/reddening variations across the field, rather than photometric errors, are the cause of the large scatter in the HB; if anything, photometric errors tend to be slightly worse in the inner region of the cluster because of crowding.

A color-color diagram of cluster HB stars is plotted in the top panel of Figure 3, while the bottom panel shows the same after correcting for reddening on a star-by-star basis. The $E(B - V)$ value for each star is taken from the SFD dust map, and an assumed R_V value of 3.0 is plugged into the CCM parameterization of the dust extinction law (Eqn. 3) to derive R_I and the corresponding $E(V - I)$ value. The reddening-corrected data (and the uncorrected data, for that matter) show

¹The Cerro Tololo Interamerican Observatory, National Optical Astronomy Observatories, is operated by the Association of Universities for Research in Astronomy, Inc. under cooperative agreement with the National Science Foundation.

a linear relationship between $B - V$ and $V - I$. A least-squares fit (solid line) is made to the reddening-corrected data:

$$(V - I) = -0.0068 + 1.27(B - V) \quad . \quad (2)$$

This equation, in conjunction with the two-polynomial fiducial fit to the HB in the $(B - V, V)$ CMD, is used to simulate BVI photometry of HB stars (§ 3.2).

2.2. Photometric Errors

Figure 4 shows the typical 1σ photometric errors in the BVI bands for NGC 4833 stars as a function of their apparent visual magnitude (Melbourne et al. 2000). The photometric errors, estimated using the DAOPHOT II software package (Stetson 1994), range from $\sigma_{\text{phot}} \sim 0.01$ mag at the bright end of the HB ($V \sim 15.5$) to $\sigma_{\text{phot}} \sim 0.05$ mag at the faint end ($V \sim 18$), and contribute noticeably to the width of the HB. The characteristic photometric error is defined to be that at $V = 17$, $\sigma_{\text{phot}}(\text{NGC 4833}) \sim 0.03$ mag, and this is what is referred to throughout the rest of this paper.

3. Simulated Cluster Data Sets

A key aspect of our study is the use of simulated cluster data sets to fine tune and test the R_V measurement methods (§ 4). These simulated data sets are designed to mimic the general properties of the NGC 4833 data set as closely as possible. Since we are also interested in applying these R_V measurement methods to a broad range of data, the main set of simulations are constructed over a two-dimensional grid of parameter space: three *input* R_V values and three levels of photometric precision. At each of these 9 (3×3) grid points, 100 Monte-Carlo realizations are carried out—i.e., a total of 900 simulated clusters are constructed each containing 260 HB stars. The rest of this section describes the step-by-step procedure used to construct each simulated data set.

3.1. Choosing Extinction Law Parameters

Three input R_V values, 2.0, 3.0 and 4.0, are chosen for the simulated cluster data sets. These mimic a range of extinction law properties for the foreground dust and span the range of values observed in lines of sight with moderate to light reddening (§ 1.1). The CCM parameterization of the Galactic extinction laws:

$$R_I \equiv A_V/E(V - I) = \frac{1}{0.32 + 0.6239/R_V}. \quad (3)$$

is adopted here. For a given choice of R_V , the visual extinction A_V is translated to its corresponding $E(B - V)$ and $E(V - I)$ color excesses.

3.2. Creating an Artificial Horizontal Branch

Each simulated star is assigned B - and V -band photometry via a random drawing from a fiducial HB curve in the CMD. The fiducial is based on stitching together two second-order polynomials that are fit to the extinction/reddening-corrected $(B - V, V)$ HB of NGC 4833, where the $E(B - V)$ correction for each star is obtained from the SFD dust map and R_V is assumed to be 3.0. Examples of such two-polynomial fiducial HBs are shown in Figures 6 and 10. The “SFD-corrected” cluster HB used for the fiducial fit is similar to the one shown in the left-middle panel of Figure 12, except for the fact that the one illustrated has had the mean extinction/reddening reapplied to it. When drawing 260 stars from the fiducial, the run of stellar density along the simulated HB is made to mimic that observed along the cluster HB. This is done by dividing the fiducial into sections and demanding that the number of stars in each section match that in the corresponding section of the cluster HB. Simulated I -band photometry is obtained from the linear fit to the $(B - V, V - I)$ color-color diagram of cluster HB stars (Fig. 3, Eqn. 2).

3.3. Modeling Reddening Variations Across the Cluster

The width of the HB can be used to quantify the effect of extinction/reddening variations. Figure 5 shows the RMS scatter of HB stars in NGC 4833 as a function of their V magnitude (solid line). The RMS scatter is calculated based on the *shortest distance* of each HB star from the fiducial curve (i.e., distance to the nearest tangent point on the curve). The fiducial consists of two second-order polynomials fit to HB stars within $2'$ of the cluster center. The dotted line in Figure 5 is a model prediction for the HB scatter that would result from photometric errors alone, the dashed line shows the effect of large-scale extinction/reddening variations from SFD plus photometric error, and the dot-dashed line the effect of small- and large-scale extinction/reddening variations plus photometric error. It is clear from the scatter at the bright end of the HB ($V \lesssim 17.5$) that only the dot-dashed line matches the NGC 4833 data. The following subsections describe in turn the simulations behind the three model lines.

3.3.1. In the Absence of Reddening Variations

A special set of 100 photometric-error-only (“ σ_{phot} -only”) simulations containing *no* reddening variations is constructed for illustration purposes only; this set is not used in any of the R_V determination exercises described in § 4. Each Monte Carlo realization in this special set involves three steps: **(1)** An artificial HB is constructed as described in § 3.2 above; **(2)** The mean extinction and reddening of the cluster, $\langle A_V \rangle = 1.0$ and $\langle E(B - V) \rangle = 0.32$ (based on $R_V = 3.0$), are applied to all simulated stars to bring them into the same range of apparent BVI magnitudes as the NGC 4833 HB stars; and **(3)** Gaussian photometric errors are added assuming $\sigma_{\text{phot}}(\text{sim}) = \sigma_{\text{phot}}(\text{NGC 4833})$. The details of step (3) are given in § 3.4 below.

The dotted line in Figure 5 is the scatter measured in 100×260 simulated HB stars. The mismatch with the NGC 4833 data (solid line) demonstrates that photometric errors alone cannot explain the width of the cluster’s HB and there must be additional sources of scatter in the HB. (The dotted line is much smoother than the solid line because it is based on $100\times$ as many stars.)

3.3.2. Large-Scale Variations

The obvious additional source of HB scatter is differential extinction/reddening across the cluster. Large-scale variations based on the SFD map are explored in this section. Their maps provide $E(B - V)$ color excesses as a function of sky position, but have an angular resolution of $\sim 6'$ and therefore contain power only on scales larger than this. The SFD map includes NGC 4833 and the region around it, and indicates that the mean reddening along this line of sight is $\langle E(B - V) \rangle \sim 0.3$ mag with variations on the order of ± 0.05 mag.

Following the procedure described above for the “ σ_{phot} -only” simulations (§ 3.3.1), another special set of 100 simulations is constructed containing only large-scale extinction/reddening variations and photometric errors. Again, these special “SFD+ σ_{phot} ” simulations are created for illustrative purposes alone. The only difference is in step (2) of the procedure: instead of applying the same (mean) extinction and reddening values to all simulated HB stars, each star is randomly assigned the sky position of one of the 260 HB stars in NGC 4833 and the corresponding SFD $E(B - V)$ value, and associated A_V and $E(V - I)$ values based on $R_V = 3.0$, are applied to the BVI magnitudes of the simulated star. By assigning actual sky positions to the simulated HB stars, we ensure that they mimic the spatial distribution of NGC 4833’s HB stars and range of large-scale extinction/reddening variations across the cluster data set.

The dashed line in Figure 5, based on 100×260 simulated HB stars, shows the scatter resulting from a realistic amount of large-scale extinction/reddening variations and photometric error. Even this line falls a little short of explaining the HB scatter observed in the cluster (solid line).

3.3.3. Small-Scale Variations

The most probable cause of this shortfall is the coarse resolution of the SFD map which averages over structure in the dust distribution on angular scales smaller than $\sim 6'$. Small-scale variations are incorporated into the simulated data sets by adding random Gaussian fluctuations with an amplitude proportional to the SFD reddening value at that location:

$$E(B - V)_{\text{LS+SS}} = E(B - V)^{\text{SFD}} [1 + f_i^{\text{SS}}] \quad (4)$$

where f_i^{SS} is a random number (for the i -th star) drawn from a Gaussian distribution with zero mean and width $\sigma^{\text{SS}} = 0.06$.

This brings us back to the main set of simulations used for testing the R_V determination methods in §4. They are constructed using a procedure similar to that used for the special set of “SFD+ σ_{phot} ” simulations (§3.3.2) but with two changes. First, the SFD reddening values in step (2) of the procedure are replaced by $E(B - V)_{\text{LS+SS}}$ from Eqn. 4 above. Second, a range of R_V values (§3.1) and photometric error levels (§3.4) are used.

With the above choice of Gaussian width for the small-scale dust variations, $\sigma^{\text{SS}} = 0.06$, and for $\sigma_{\text{phot}}(\text{sim}) = \sigma_{\text{phot}}(\text{NGC 4833})$ and $R_V = 3.0$, the scatter in the simulated HB approaches that of NGC 4833’s HB (dot-dashed vs. solid lines in Fig. 5). This is a reasonable estimate of the amount of smoothing of dust fine-scale structure in the SFD maps (§5.1; Fig. 14), and is well within the 10% uncertainty in reddening values estimated by the authors.

3.4. Accounting for Photometric Error

The final step in the construction of the main set of simulated HB data sets is the inclusion of photometric error. Since the photometric uncertainty is a function of stellar brightness, this step must be carried out after the inclusion of (large- and small-scale) dust effects so that each star is at the appropriate apparent brightness. Gaussian random noise is added to the BVI magnitudes of each star. Three levels of photometric error are simulated: (1) $\sigma_{\text{phot}}(\text{sim}) = \sigma_{\text{phot}}(\text{NGC 4833})$, with the latter being the DAOPHOT-based errors shown in Figure 4; (2) $\sigma_{\text{phot}}(\text{sim}) = 0.5 \sigma_{\text{phot}}(\text{NGC 4833})$; and (3) $\sigma_{\text{phot}}(\text{sim}) = 0.1 \sigma_{\text{phot}}(\text{NGC 4833})$.

4. Measuring R_V

We employ three methods for measuring R_V in the direction of differentially-reddened globular clusters. Each method relies on the premise that the width of the blue HB will be minimized when the appropriate R_V value is used to correct for extinction and reddening. A description of each method and its application to the NGC 4833 and simulated cluster data sets follows.

4.1. A_V RMS Method

4.1.1. Description of Technique

The “ A_V RMS” method relies on three-color photometry of differentially-reddened globular clusters. Figure 6 shows the $(B - V, V)$ and $(V - I, V)$ CMDs of a simulated HB (left and right panels, respectively). A fiducial, consisting of two second-order polynomials stitched together (solid curve; §3.2), is fit to the HB stars within $2'$ of the cluster center where differential extinction/reddening is relatively small; this is done independently for the $(B - V, V)$ and $(V - I, V)$ CMDs. The relative visual extinction of each star is calculated to be the vertical distance between

the star and the point where the reddening vector drawn from the star intersects the fiducial (Fig. 6 inset); it is designated $(\delta A_V)^{BV}$ and $(\delta A_V)^{VI}$ for the $(B - V, V)$ and $(V - I, V)$ CMDs, respectively.² The $(\delta A_V)^{BV}$ measurement is based on an assumed/test value of R_V , the slope of the reddening vector in the $(B - V, V)$ CMD. For the $(\delta A_V)^{VI}$ calculation, the CCM parameterization given in Eqn. 3 is used to translate R_V to R_I , the slope in the $(V - I, V)$ CMD.

The difference between the two δA_V values is defined to be $(\Delta A_V)^{BV,VI} \equiv (\delta A_V)^{BV} - (\delta A_V)^{VI}$. For a given test value of R_V , the RMS scatter of $(\Delta A_V)^{BV,VI}$ is computed over all HB stars. This is done in two iterations, with $3\text{-}\sigma$ rejection of outliers after the first iteration to eliminate any non-HB stars in the sample (e.g., cluster blue stragglers or Galactic field main sequence turnoff stars in the foreground—encircled symbols in upper panels of Fig. 2). Non-HB interlopers are expected to have large deviations from the HB fiducial with effective δA_V values that are different between the two CMDs.

The calculation of the RMS of $(\Delta A_V)^{BV,VI}$ is repeated for a series of test R_V values between 0.5 and 5.5 in steps of 0.25. The δA_V parameters from the two CMDs are expected to approach each other when the test value approaches the true R_V of the dust in the foreground of the cluster. In other words, the RMS of $(\Delta A_V)^{BV,VI}$ should go through a minimum at the correct R_V value. A polynomial fit is made to the RMS of $(\Delta A_V)^{BV,VI}$ vs. test R_V data points to interpolate to the minimum.

4.1.2. Application to Data and Simulations

Figure 7 shows the RMS scatter in $(\Delta A_V)^{BV,VI}$ vs. test R_V value, the result of applying the A_V RMS method to NGC 4833 (filled diamonds) and three sample simulated cluster data sets (open triangles). The simulated data sets are all based on an input R_V value of 3.0, but have different levels of photometric error: 10%, 50%, and 100% that of the NGC 4833 data set (§ 3.4), with the RMS sequences arranged in order of $\sigma_{\text{phot}}(\text{sim})$ increasing upwards. As expected, each sequence of RMS of $(\Delta A_V)^{BV,VI}$ vs. test R_V goes through a clear minimum (large open square) near $R_V = 3.0$. The depth/sharpness of the RMS minimum decreases with increasing photometric error and the power of the method diminishes.

The results for all 9×100 simulated cluster data sets are summarized in Table 1. For $\sigma_{\text{phot}}(\text{sim}) = 0.1 \sigma_{\text{phot}}(\text{NGC 4833})$, the A_V RMS method reproduces the correct R_V to within ± 0.1 , as measured by the standard deviation of measured (output) R_V values for 100 simulated data sets. The scatter in output R_V increases to ± 0.7 for $\sigma_{\text{phot}}(\text{sim}) = \sigma_{\text{phot}}(\text{NGC 4833})$. The (absolute) precision of the method appears to decrease with increasing input R_V , again judging

²Throughout this paper, the symbol “ δA_V ” is used to denote the relative visual extinction of a star based on a single fiducial/CMD, whereas “ ΔA_V ” is used to denote the *difference* between two δA_V values, say between two CMDs for a given star or between a pair of stars.

from the scatter of output R_V values, although the fractional error $\sigma(R_V)/R_V$ remains roughly constant. It is important to note that the output R_V from this method tends to be biased low for moderate to large photometric errors and input $R_V \gtrsim 3$. For example, simulated data sets with input $R_V = 3.0$ and $\sigma_{\text{phot}}(\text{sim}) = \sigma_{\text{phot}}(\text{NGC 4833})$ (a good match to the real cluster data) have a mean output $\langle R_V \rangle = 2.60 \pm 0.7$. This bias of -0.4 in $\langle R_V \rangle$ is significant compared to the error in the mean, $0.7/\sqrt{100} = 0.07$, and must be taken into account in the determination of R_V for an actual cluster data set.

The cause of the bias towards low R_V may be explained as follows. Photometric error produces scatter in the HB which, unlike the scatter caused by variable extinction/reddening, is *uncorrelated* between the two CMDs—i.e., the resulting values of $(\delta A_V)^{BV}$ and $(\delta A_V)^{VI}$ are different. These errors are particularly important at faint magnitudes where the HB is vertical and the effect is a spread in color. All else being equal, choosing a smaller R_V (and R_I) translates these color errors into smaller δA_V values and hence to smaller $(\Delta A_V)^{BV,VI}$ differences as well. This biases the RMS minimum towards lower R_V values.

The RMS of $(\Delta A_V)^{BV,VI}$ for the NGC 4833 data set displays a significant minimum at $R_V = 2.5 \pm 0.7$ (open square associated with filled diamonds in Fig. 7), where the error bar is taken directly from the scatter in output R_V for comparable simulated data sets. Correcting for the bias in the measured $\langle R_V \rangle$ for such simulations, our best guess for the R_V towards NGC 4833 is 2.9 ± 0.7 .

4.2. A_V Slope Method

4.2.1. Description of Technique

The “ A_V Slope” method is closely related to the A_V RMS method in that it relies on the same $(\delta A_V)^{BV}$ and $(\delta A_V)^{VI}$ values determined for each star in § 4.1.1 above. Instead of computing the difference between the two δA_V values as in the A_V RMS method, one is plotted against the other and a linear fit made. This is illustrated in Figure 8 for a simulated cluster data set created with (input) $R_V = 3.0$; four test R_V values are shown. The linear fit in each panel is effectively a bivariate one: one of the dashed lines is a fit treating the x - and y -axes as the independent and dependent variables, respectively, and vice versa for the other dashed line; their slopes are averaged to get the solid line. As expected, the slope of the linear fit approaches unity when the test R_V approaches the true (input) R_V value. As in § 4.1.1, a polynomial fit is made to the slope vs. test R_V data to interpolate to unit slope.

4.2.2. Application to Data and Simulations

Figure 9 shows results from the application of the A_V Slope method: the slope of the relation between $(\delta A_V)^{BV}$ and $(\delta A_V)^{VI}$ is plotted versus test R_V . The format of this figure is the same as for Figure 7, except that a slope of unity (rather than an RMS minimum) corresponds to the best-fit R_V value. The A_V Slope method results for NGC 4833 and simulated data sets are summarized in Table 1.

Applying this method to 9×100 simulated data sets, we learn that, like the A_V RMS method, the power of the A_V Slope method decreases with increasing photometric errors. The scatter in output R_V is ± 0.1 for $\sigma_{\text{phot}}(\text{sim}) = 0.1 \sigma_{\text{phot}}(\text{NGC 4833})$, but increases to ± 0.6 for $\sigma_{\text{phot}}(\text{sim}) = \sigma_{\text{phot}}(\text{NGC 4833})$. Some of the 9 simulation categories display a small but significant bias (positive or negative) in the measured (output) $\langle R_V \rangle$, but not the category directly relevant to NGC 4833. The cause of this bias is not as readily apparent as for the “ A_V RMS” method (§ 4.1.2). For the NGC 4833 data set, the A_V Slope method gives $R_V = 2.6 \pm 0.6$.

4.3. Optical/IR Method

4.3.1. Description of Technique

The “Optical/IR” method is different from the previous two methods in that it relies on two-color photometry (i.e., a single CMD which, in our case, is V vs. $B - V$) and the SFD reddening map. Using a test R_V value, A_V values are derived for all HB stars by scaling the corresponding SFD $E(B - V)$ values. These color and magnitude corrections are applied on a star-by-star basis. Figure 10 shows the $(B - V, V)$ CMD of a simulated HB before (left) and after (right) making the extinction/reddening corrections. The latter HB is slightly tighter, but not dramatically so because the SFD reddening values smooth over small-scale dust variations. The RMS scatter of the corrected HB stars is computed with respect to a best-fit fiducial curve (two second-order polynomials—solid line in Fig. 10) based on “shortest distance” (see § 3.3). This process is repeated for a range of test R_V values as for the other two methods. The RMS scatter is expected to go through a minimum when the test R_V approaches the true R_V value. As in § 4.1.1, a polynomial fit is made to the HB scatter vs. test R_V data to interpolate to the minimum.

4.3.2. Application to Data and Simulations

Figure 11 shows results from the application of the Optical/IR method: RMS scatter of HB stars versus test R_V . The format of this figure is the same as for Figure 7. The Optical/IR results for NGC 4833 and simulated data sets are summarized in Table 1.

Tests of the method on 9×100 simulated cluster data sets indicate that the method has a

low level of predictive power ($\sim \pm 0.6$ in R_V) over the full range of photometric errors simulated. This is because the main source of error here is uncertainty in the SFD reddening values, including small-scale dust variations that get smoothed out by the relatively coarse resolution of their map. The Optical/IR method gives $R_V = 3.5 \pm 0.7$ for NGC 4833.

4.4. Discussion

Our best estimate of the extinction law slope in the direction of NGC 4833 is $R_V = 3.0 \pm 0.4$, based on a weighted average of the values from the three determination methods (see Table 1). Before averaging, the output R_V value from the A_V RMS method is corrected for measurement bias: $2.5 \rightarrow 2.9$ (§ 4.1.2). The weights are proportional to $1/[\sigma(R_V)]^2$ where $\sigma(R_V)$ is the uncertainty in output R_V for a given determination method as derived from the simulations.

Figure 12 illustrates the effectiveness of the star-by-star extinction/reddening corrections based on the R_V determination methods described earlier in this section. The top two panels show the uncorrected NGC 4833 HB in the $(B - V, V)$ and $(V - I, V)$ CMDs (left and right panels, respectively). The photometry in the middle two panels has been corrected for extinction/reddening based on the SFD $E(B - V)$ maps, using a best-fit $R_V = 3.0$ and the corresponding R_I from Eqn. 3 to translate the $B - V$ color excess to A_V and $E(V - I)$. Note, the mean extinction and reddening of the cluster have been added back to the data for ease of comparison with the top panels. The HB is somewhat tighter after the SFD-based correction but the effect is fairly subtle, a result of missing small-scale dust structure in the SFD map and possibly other sources of uncertainty as well.

The correction in the bottom two panels of Figure 12 is based on information derived from BVI photometry of the cluster HB. The relative visual extinction measures derived from the two CMDs, $(\delta A_V)^{BV}$ and $(\delta A_V)^{VI}$ (§ 4.1.1), are averaged to obtain a $\langle \delta A_V \rangle$ value for each HB star. This is translated to color excesses in the two CMDs using the best-fit $R_V = 3.0$ and its corresponding R_I (Eqn. 3). The dramatic tightening of the HB indicates that the scatter is strongly correlated between $(B - V, V)$ and $(V - I, V)$ CMDs—e.g., if a star is displaced to the right of/below the HB fiducial in one CMD, it tends to be displaced in the same direction and by the same amount (or by a proportional amount in color) in the other CMD. The most natural explanation of this correlated HB scatter is of course differential extinction/reddening in the NGC 4833 data set.

There is a handful of stars at each extremity of the HB in the bottom two panels of Figure 12 that do not follow the tight sequence delineated by the rest of the stars—in fact, their scatter is unchanged relative to the uncorrected CMDs in the top panels. This is because the polynomial HB fiducial used to determine δA_V does not extend all the way to the ends of the sequence (to avoid extrapolation of the fit); as a result no δA_V measurement or correction is available for these stars. A couple of stars near the middle of the HB continue to show large deviations in the δA_V -corrected CMDs but these are probably non-HB stars (see § 4.1.1 and Fig. 2).

Before closing out this discussion, two additional sources of HB scatter are considered. The first of these is photometric error. Errors in B and I magnitudes produce uncorrelated shifts between the two CMDs. Errors in V produce shifts with slope -1 in the $(B - V, V)$ CMD, more or less orthogonal to the reddening vector, and shifts of slope $+1$ in the $(V - I, V)$ CMD, roughly along the reddening vector though its slope R_I is significantly steeper than unity. Only at the very top of the HB where it becomes horizontal can V magnitude errors mimic differential extinction/reddening effects. To summarize, photometric errors cannot explain the correlated scatter seen in NGC 4833’s HB. Moreover, as will be demonstrated in § 5, the difference in δA_V between pairs of HB stars scales with their angular separation in a manner consistent with the dust power spectrum measured at larger angular separations; photometric errors have no natural way of explaining this trend either.

Another factor to consider is *intrinsic* scatter in the HB caused by astrophysical effects such as variations in chemical abundance, age, and mass loss between cluster stars. It is possible that these can produce correlated scatter between the two CMDs and thereby mimic differential extinction/reddening. However, this scenario cannot explain the scaling of the δA_V differences with angular separation (§ 5). If there was a radial gradient in intrinsic stellar properties within the cluster, one might expect to see a shift of the HB sequence in the CMD between inner and outer regions. Instead, Figure 2 shows no such shift (the increased scatter in the HB in the outer CMD is best explained in terms of dust variations; see § 2.1).

5. Angular Power Spectrum of the Cirrus

In earlier sections, we demonstrated the effects of spatial extinction/reddening variations on the photometry of NGC 4833. We now turn to a statistical description of the strength of these extinction/reddening variations as a function of angular scale. Figure 13 is a map of the *relative* visual extinction across the face of NGC 4833. Each point on the map represents the sky position of a HB star in the cluster. The size of each point is scaled by the measured strength of the relative visual extinction $(\delta A_V)^{BV}$ at that location; it varies from -0.20 to $+0.37$ mag (smallest \rightarrow largest). As described in § 4.1.1, $(\delta A_V)^{BV}$ is the vertical distance between the star’s CMD location and the point where the reddening vector drawn from the star intersects the fiducial HB; the fiducial is a fit to the central region of the cluster, and therefore corresponds to a mean visual extinction of $\langle A_V \rangle \sim 1$. In keeping with the findings of Melbourne et al. (2000), there is a clear overall N-S gradient in $(\delta A_V)^{BV}$ across NGC 4833, but the extinction can vary significantly from point to point even for points relatively close to each other.

These variations can be characterized in terms of the angular power spectrum of the foreground dust complex. A direct measurement of the power spectrum is difficult however because of the sparse and irregular spatial sampling of the data points. The following approach is adopted instead. First, the “variance spectrum” as a function of angular scale is calculated from the cluster $(\delta A_V)^{BV}$ data (§ 5.1). Next, a variance spectrum and conventional power spectrum are measured from the uniformly-sampled SFD maps, and an empirical transformation is calculated from the former to

the latter (§ 5.2). Finally, this empirical transformation is applied to the cluster variance spectrum to convert it to a power spectrum, and this allows us to study the composite power spectrum over a wide range of angular scales (§ 5.3).

5.1. Variance versus Angular Separation from NGC 4833 Optical Data

The best-fit value of $R_V = 3.0$ for NGC 4833 is used to determine the relative visual extinction corresponding to the i -th HB star, $(\delta A_V)_i^{BV}$. The difference in relative A_V between stars i and j , $(\Delta A_V)_{ij}^{BV} \equiv (\delta A_V)_i^{BV} - (\delta A_V)_j^{BV}$, and their angular separation r_{ij} are then calculated for all possible pairs of HB stars. Figure 14 (open diamonds) shows the variance (mean square deviation) of $(\Delta A_V)_{ij}^{BV}$ as a function of angular separation r in a log-log plot; the radial bins are chosen so as to include roughly equal numbers of pairs in each bin. The variance decreases with decreasing r before levelling off at $\log[\text{var}[(\Delta A_V)_{ij}^{BV}]] = -2.3$ for $r \lesssim 100''$. The behavior at low r may be attributed to photometric errors and possibly the natural width of the HB.

In order to quantify and compensate for the effect of photometric error on the variance spectrum, we resort to the special set of “ σ_{phot} -only” simulations containing *no* reddening variations (§ 3.3.1). The variance of this “ σ_{phot} -only” simulated data set, analyzed in the same way as the real cluster data set, is: $\log[\text{var}[(\Delta A_V)_{ij}^{BV}]] = -2.4$, and is of course independent of stellar angular separation (dashed horizontal line in Fig. 14). The variance due to photometric errors is subtracted from the variance spectrum of NGC 4833, equivalent to statistical subtraction of errors in quadrature. The resulting variance spectrum is shown as filled diamonds in Figure 14. A power-law fit to the corrected variance spectrum:

$$\text{var}(r) \propto r^\beta, \quad (5)$$

yields an index of $\beta = +0.9 \pm 0.1$, over the radial range $50''$ – $300''$. The upper end of this range corresponds to the Nyquist frequency of the $13.5' \times 13.5'$ area covered by the NGC 4833 data set. The first radial bin of the corrected variance spectrum ($r < 50''$) is excluded from the power-law fit because it is strongly affected by uncertainties in the photometric error correction.

The cluster variance spectrum is used to make a rough estimate of how much small-scale power is missing from the SFD dust map. The SFD map, like the IRAS $100 \mu\text{m}$ data on which they are based, have an angular resolution of about $6'$, or $\log(r) \sim 2.6$. This point in the cluster variance spectrum corresponds to $\text{var}[(\Delta A_V)_{ij}^{BV}] = 4.4 \times 10^{-3}$. The RMS scatter at this point is $\sqrt{\text{var}[(\Delta A_V)_{ij}^{BV}]} = 6.6 \times 10^{-2}$. Since the mean visual extinction $\langle A_V \rangle \approx 1$ in the direction of NGC 4833, the RMS is about 7% of the mean. This provides a good sanity check: it corroborates the result from the analysis of the cluster HB width (§ 3.3.2) that the SFD map is missing small-scale variations on the order of 6% of the reported reddening value. It also gives an indication of how accurately one can correct for extinction/reddening using the SFD map, with general implications for precision photometry in dusty regions of the sky.

5.2. Variance and Power Spectra from SFD Map

In this section, the SFD map is used to investigate the relationship between the variance spectrum and conventional angular power spectrum. This is done by extracting a $10^\circ \times 10^\circ$ SFD reddening image centered on NGC 4833. The $E(B - V)^{\text{SFD}}$ reddening values are converted to A_V using the best-fit R_V of 3.0. The difference in visual extinction between pixels i and j , $(\Delta A_V)_{ij}^{\text{SFD}} \equiv (\Delta A_V)_i^{\text{SFD}} - (\Delta A_V)_j^{\text{SFD}}$, is calculated for all possible pairs of pixels. The variance of $(\Delta A_V)_{ij}^{\text{SFD}}$ is computed as a function of angular separation r . The ‘+’ symbols in Figure 15 show $\text{var}(\kappa)/\kappa$ for the SFD map, where $\kappa \equiv 1/r$.

The two-dimensional power spectrum of dust fluctuations is computed via a Fast Fourier Transform (FFT) of the SFD reddening image. This is then azimuthally averaged to produce a one-dimensional angular power spectrum $P(\kappa)$, shown by asterisks in Figure 15. Over the radial range $r = 10'$ to 1° [$\log(\kappa) \sim -2.8$ to -3.6], $\text{var}(\kappa)/\kappa$ and $P(\kappa)$ have comparable logarithmic slopes (power-law index: $\alpha \approx -2.0 \pm 0.1$) such that:

$$\text{var}(\kappa)/\kappa \approx C P(\kappa) \tag{6}$$

with a best-fit scale factor of $\log(C) = -4.3$.

5.3. Composite Power Spectrum of the Cirrus

The above transformation (Eqn. 6) is applied to the photometric-error-corrected variance spectrum derived from the NGC 4833 BV data (§ 5.1) to convert it to an angular power spectrum. The result is shown as filled diamonds in Figure 15. This small-scale power spectrum derived from optical data matches smoothly onto the power spectrum derived from the SFD map at larger angular scales. A power law with an index $\alpha \sim -2.0$ provides an adequate fit to the data over the full range of projected separations shown in Figure 15, $r \sim 1'$ to 3° .

Our best-fit index α is significantly shallower than the index of -3 found by Gautier et al. (1992) and Guhathakurta & Cutri (1994) and at the shallow end of the range of indices found by Kiss et al. (2003) in their ISOPHOT-based study of 13 fields: $\alpha \sim -2.1$ to -5.3 (± 0.1). The shallower the power-spectrum index, the larger the *fraction* of power missed by the SFD map on small scales relative to that on larger scales. Another possible implication relates to Kiss et al.’s finding that shallower α values are associated either with low HI column density, $N_{\text{HI}} < 10^{21} \text{ cm}^{-2}$, and/or warm dust. For example, in the region of the Draco Nebula, they find that the map of $90 \mu\text{m}$ emission (dominated by warmer dust) yields $\alpha = -2.5 \pm 0.2$ while the $170 \mu\text{m}$ map (dominated by cooler dust) yields $\alpha = -4.1 \pm 0.2$.

6. Future Work

While NGC 4833 has an extended blue HB, the methods presented in this paper should be usable for clump HBs or the RGB or any other tight CMD feature for that matter. For instance, Law et al. (2003) used the width of the RGB to measure differential reddening in the direction of three Galactic globular clusters, von Braun et al. (2002) used the main sequence for their study, and Udalski (2003) used clump stars to probe dust along the line of sight to the Galactic bulge. Our methods should work for any three bands, not just *BVI*. Additional bands (beyond three) can provide: (1) a longer wavelength baseline and therefore more leverage in R_V determination; (2) a larger number of independent measures of the star-by-star extinction/reddening which can be averaged to beat down the errors; and (3) most importantly, an empirical check of the CCM parameterization of the shapes of Galactic extinction laws.

There is at least one generalization of the methodology presented here that might be worth exploring in the future. In determining δA_V , we effectively use V magnitude to mark where along the HB sequence the extinction/reddening-corrected star lies. A more general definition of a “locator” parameter, to mark the position of the unreddened star along any given CMD sequence, may be particularly useful. For example, multi-wavelength data sets may not have any single observable in common across all of the CMDs in question (unlike the V mag for our two CMDs), and a color parameter may be more sensitive than V mag when using a not-so-vertical CMD feature (such as the upper portion of NGC 4833’s HB).

Several high-quality, multi-band (three or more), ground- and space-based photometric data sets have long been available for many star clusters, so the methods presented here can be readily implemented to probe the nature of dust along many lines of sight. These include Milky Way clusters, as well as others near enough to allow clean photometry in relatively uncrowded fields, such as *Hubble Space Telescope* images of clusters in, and even somewhat beyond, the Magellanic Clouds. Many of these clusters have detectable extinction/reddening variations across them—e.g., ω Centauri, NGC 6388, NGC 6441 (Law et al. 2003), M10, and M12 (von Braun et al. 2002). The Sloan Digital Sky Survey (SDSS, Stoughton et al. 2002) five-band ($u'g'r'i'z'$) data set, with its high photometric accuracy, minimal systematic errors, excellent uniformity/homogeneity, and large areal coverage, is opening up lines of sight towards differentially-reddened star clusters across the entire high-latitude North Galactic cap for this type of analysis. Near-infrared *JHK* photometry from the Two Micron All-Sky Survey (2MASS) data should also prove very fruitful, both for probing highly-reddened lines of sight and for extending the SDSS wavelength coverage. Making R_V and power spectrum measurements along many sight-lines should lead to a better understanding of grain formation and chemistry and the effect of interstellar dust on astronomical observations.

While our 3×3 grid of simulations covers some amount of parameter space in photometric error and R_V , it is fairly limited in scope: it cannot simply be translated to any arbitrary cluster data set. Another data set may be different from the NGC 4833 data set in terms of photometric bandpasses, level of photometric error, areal coverage, detailed morphology of CMD features, degree

of extinction/reddening variations, and/or extinction law slope. New simulations must be carried out, matched to the exact parameters of each new cluster data set in question, in order to test the efficacy of the R_V measurement methods presented here.

7. Conclusions

- We have demonstrated the use of three methods, “ A_V RMS”, “ A_V Slope”, and “Optical/IR” methods, for determining the dust extinction law slope R_V in the direction of differentially-reddened Galactic globular clusters, and have tested the methods on an extensive suite of simulated cluster data sets.
- For cluster data sets with low photometric error, $\sigma_{\text{phot}} \lesssim 0.01$ mag, the “ A_V RMS” and “ A_V Slope” methods can be used to determine R_V to an accuracy of $\sigma(R_V) = 0.1\text{--}0.3$. For cluster data sets with $\sigma_{\text{phot}} \gtrsim 0.03$ mag, the two methods yield R_V to within ± 0.7 , with some systematic biases.
- The “Optical/IR” method generally provides relatively imprecise estimates of R_V , $\sigma(R_V) \sim 0.6$, over the full range of photometric errors explored.
- Combining the results from all three methods gives a mean extinction law slope of $R_V = 3.0 \pm 0.4$ for the line of sight towards the low-latitude Galactic globular cluster NGC 4833.
- The scatter in the cluster HB is used to estimate the amount of small-scale structure in the dust complex in the foreground of NGC 4833. The Schlegel et al. (1998) IRAS+DIRBE-based map of the dust thermal emission averages over small-scale reddening variations that are $\approx 6\%$ of the mean reddening value.
- Star-to-star variations in relative visual extinction across the face of NGC 4833 provide a measure of the foreground dust angular power spectrum for projected separations in the range $r \sim 1'\text{--}5'$. This small-scale power spectrum derived from cluster optical data matches smoothly onto the larger-scale power spectrum derived from the SFD reddening map of the region. The overall power spectrum is well fit by a power law: $P(\kappa) \propto \kappa^\alpha$, where κ is the reciprocal of the angular scale r , with spectral index $\alpha \approx -2.0 \pm 0.1$.

We would like to thank Neil Balmforth, David Burstein, Sandra Faber, and Peter Stetson for comments that significantly improved this work. We would also like to thank Ata Sarajedini for providing the observations of NGC 4833.

REFERENCES

Barbaro, G., Mazzei, P., Morbidelli, L., Patriarchi, P., & Perinotto, M. 2001, *A&A*, 365, 157

- Beichman, C. A. 1987, *ARA&A*, 25, 521
- Cardelli, J. A., Clayton, G. C., & Mathis, J. S. 1989, *ApJ*, 345, 245 (CCM)
- Fitzpatrick, E. L. 1999, *PASP*, 111, 63
- Fitzpatrick, E. L., & Massa, D. 1990, *ApJS*, 72, 163
- Gautier, T. N., Boulanger, F., Perault, M., & Puget, J. L. 1992, *AJ*, 103, 1313
- Guhathakurta, P., & Cutri, R. M. 1994, in *The First Symposium on the Infrared Cirrus and Diffuse Interstellar Clouds*, eds. R. M. Cutri & W. B. Latter (ASP Conf. Ser., Vol. 58), 34
- Herbstmeier, U., et al. 1998, *A&A*, 332, 739
- Kiss, Cs., Ábrahám, P., Klaas, U., Lemke, D., Héraudeau, Ph., del Burgo, C., & Herbstmeier, U. 2003, *A&A*, 399, 177
- Larson, K. A., Whittet, D. C. B., & Hough, J. H. 1996, *ApJ*, 472, 755
- Law, D. R., Majewski, S. R., Skrutskie, M. F., Carpenter, J. M., & Ayub, H. F. 2003, *AJ*, 126, 1871
- Low, F. J., et al. 1984, *ApJ*, 278, L19
- Mathis, J. S. 1990a, *ARA&A*, 28, 37
- Mathis, J. S. 1990b, *ASP Conf. Ser. 12: The Evolution of the Interstellar Medium*, 63
- Melbourne, J., Sarajedini, A., Layden, A., & Martins, D. H. 2000, *AJ*, 120, 3127
- Mihalas, D., & Routly, P. M. 1968, *A Series of Books in Astronomy and Astrophysics* (San Francisco: W. H. Freeman and Co.)
- Popowski, P. 2000, *ApJ*, 528, L9
- Popowski, P. 2004, in preparation
- Popowski, P., Cook, K. H., & Becker, A. C. 2003, *AJ*, 126, 2910
- Rhoads, J. E., Malhotra, S., & Kochanski, G. P. 2004, in preparation
- Savage, B. D., & Mathis, J. S. 1979, *ARA&A*, 17, 73
- Schlegel, D. J., Finkbeiner, D. P., & Davis, M. 1998, *ApJ*, 500, 525
- Stetson, P. B. 1994, *PASP*, 106, 250
- Stoughton, C., Lupton, R. H., Bernardi, M., et al. 2002, *AJ*, 123, 485
- Sumi, T. 2004, *MNRAS*, in press (astro-ph/0309206)
- Szomoru, A., & Guhathakurta, P. 1999, *AJ*, 117, 2226
- Udalski, A. 2003, *ApJ*, 590, 284
- von Braun, K., Mateo, M., Chiboucas, K., Athey, A., & Hurley-Keller, D. 2002, *AJ*, 124, 2067
- Whitford, A. E. 1958, *AJ*, 63, 201

Whittet, D. C. B., Gerakines, P. A., Hough, J. H., & Shenoy, S. S. 2001, *ApJ*, 547, 872

Witt, A. N. 2003 (editor), *Astrophysics of Dust* (Estes Park, Colorado)

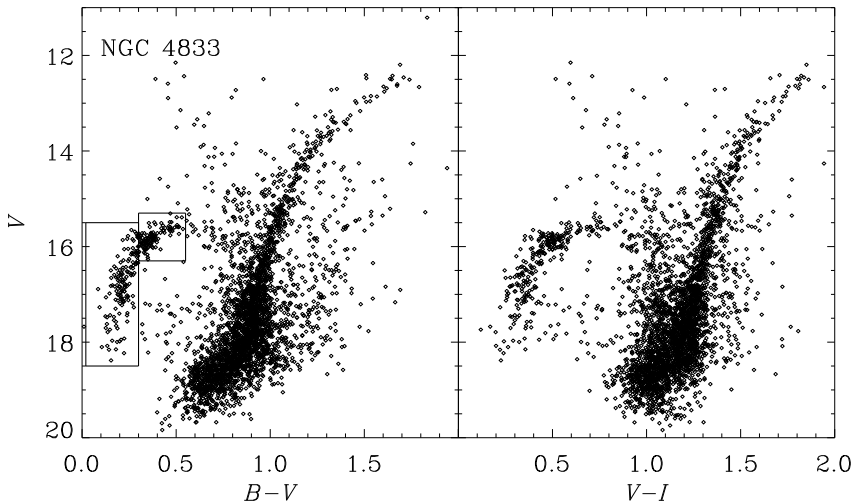


Fig. 1.— Color-magnitude diagrams in V vs. $B - V$ (left) and V vs. $V - I$ (right) of a $13.5' \times 13.5'$ field centered on the low-latitude Galactic globular cluster NGC 4833. Note the prominent curved blue horizontal branch. The boxes in the $(B - V, V)$ CMD are used to select 260 candidate cluster HB stars; the analysis presented in this paper is based solely on this subset of stars.

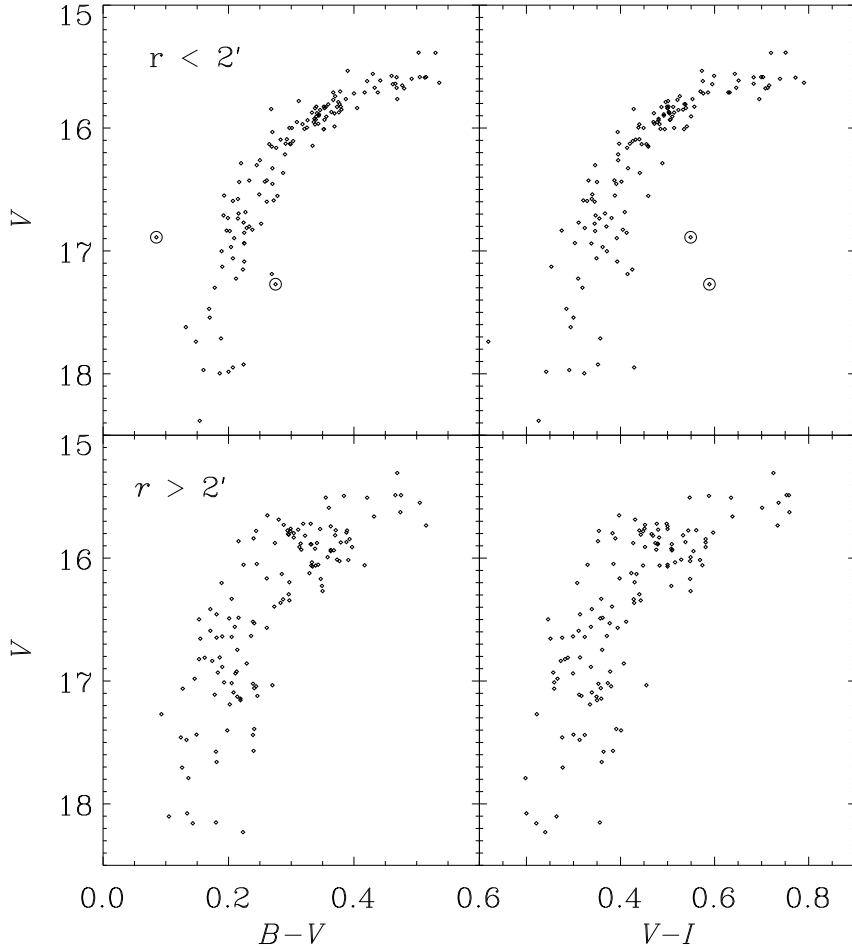


Fig. 2.— Same as Figure 1, except only candidate HB stars are shown, divided into two groups based on their projected distance from the cluster center: $r < 2'$ (upper panels) and $r > 2'$ (lower panels). The HBs are tighter in the central CMDs because they are based on a relatively small area of the sky across which there is not much differential extinction/reddening. By contrast, the HBs in the lower panels are significantly broadened by the effects of differential extinction/reddening; as a result, the scatter ‘pattern’ is similar between left and right CMDs. The two encircled dots in the upper panels may be non-HB stars (§ 4.1.1).

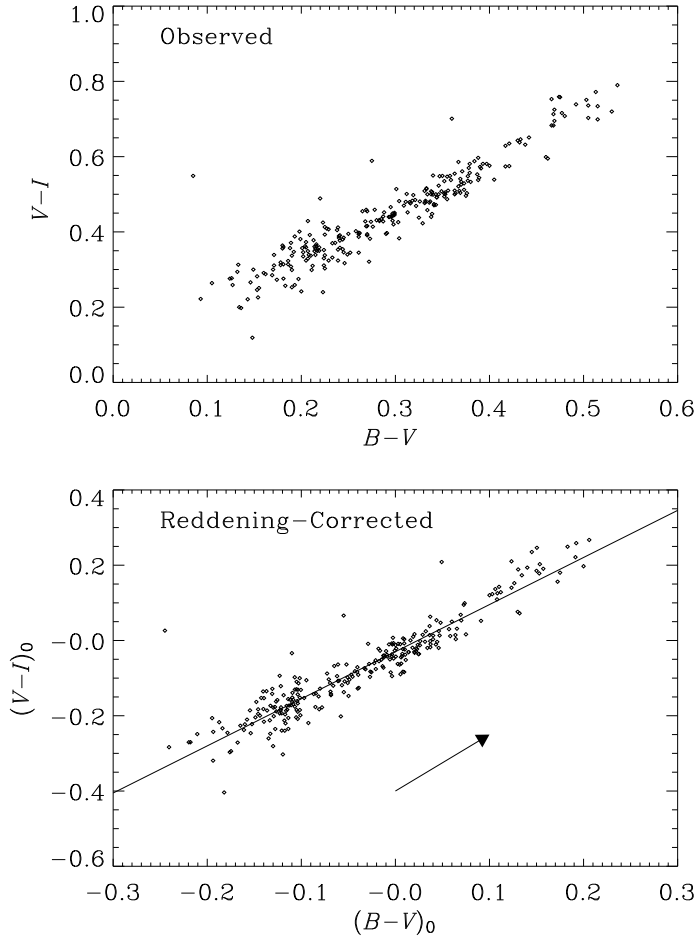


Fig. 3.— The $B - V$ versus $V - I$ color-color diagram of NGC 4833 before (top) and after (bottom) correcting for differential reddening. The correction is taken from the Schlegel et al. (1998) dust maps with $R_V = 3.0$. The solid line is a least-squares linear fit to the reddening-corrected data; it is used in the construction of artificial HBs for simulated cluster data sets. The arrow indicates the direction of the reddening vector. The reddening-corrected sequence is only marginally tighter than the uncorrected one; the change is subtle because the SFD map averages over small-scale dust variations and the reddening vector runs nearly parallel to the sequence.

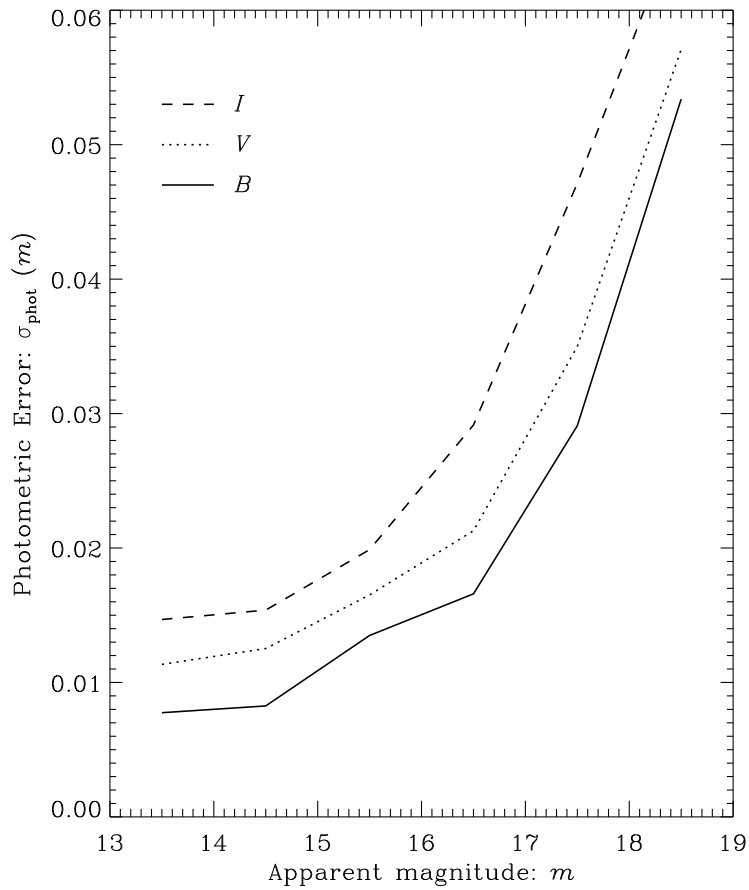


Fig. 4.— The mean 1σ photometric errors of HB stars in the NGC 4833 data set are plotted as a function of apparent magnitude m in the B , V , and I bands. The errors were derived from the DAOPHOT II (Stetson 1994) PSF-fitting routines as described in Melbourne et al. (2000).

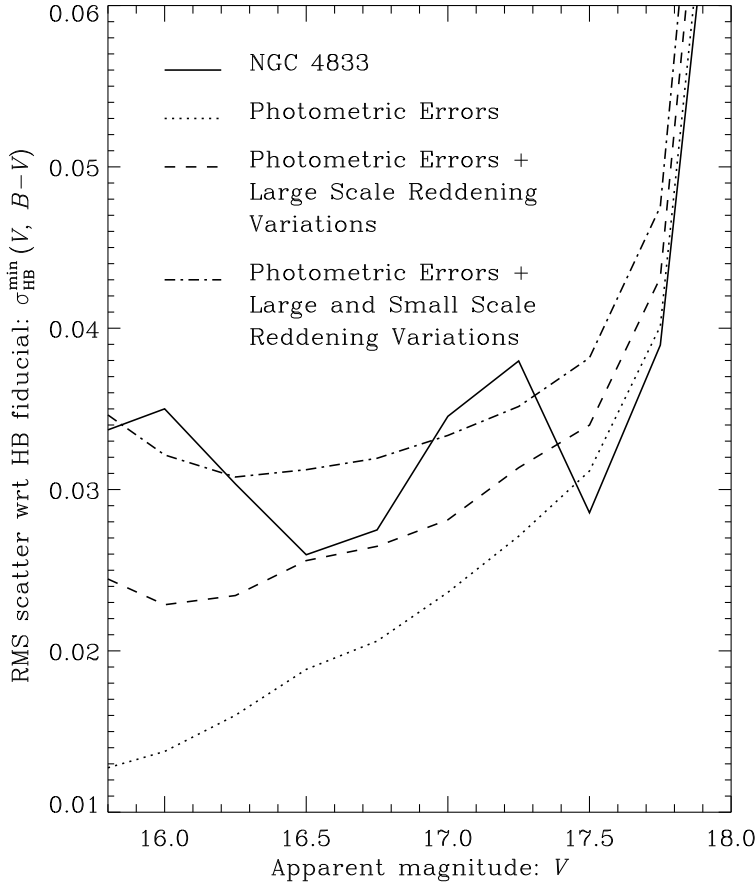


Fig. 5.— The RMS scatter of NGC 4833’s HB stars, based on “shortest distance” from a fiducial line in the $(B - V, V)$ CMD (§ 3.3), as a function of V magnitude (solid line). Each smooth curve represents 100 simulated cluster data sets. The dotted line is based on the special “ $\sigma_{\text{phot-only}}$ ” simulations (§ 3.3.1) constructed with mean extinction/reddening and photometric errors similar to those of NGC 4833, but with *no* spatial reddening variations. The dashed line is based on the special “SFD+ σ_{phot} ” simulations (§ 3.3.2) that also include large-scale extinction/reddening variations from the Schlegel et al. (1998) map. The dot-dashed line is based on simulations that include large- and small-scale extinction/reddening variations and photometric error (§ 3.3.3); all three factors are needed to explain the scatter seen in the bright portion ($V \lesssim 17.5$) of the cluster HB.

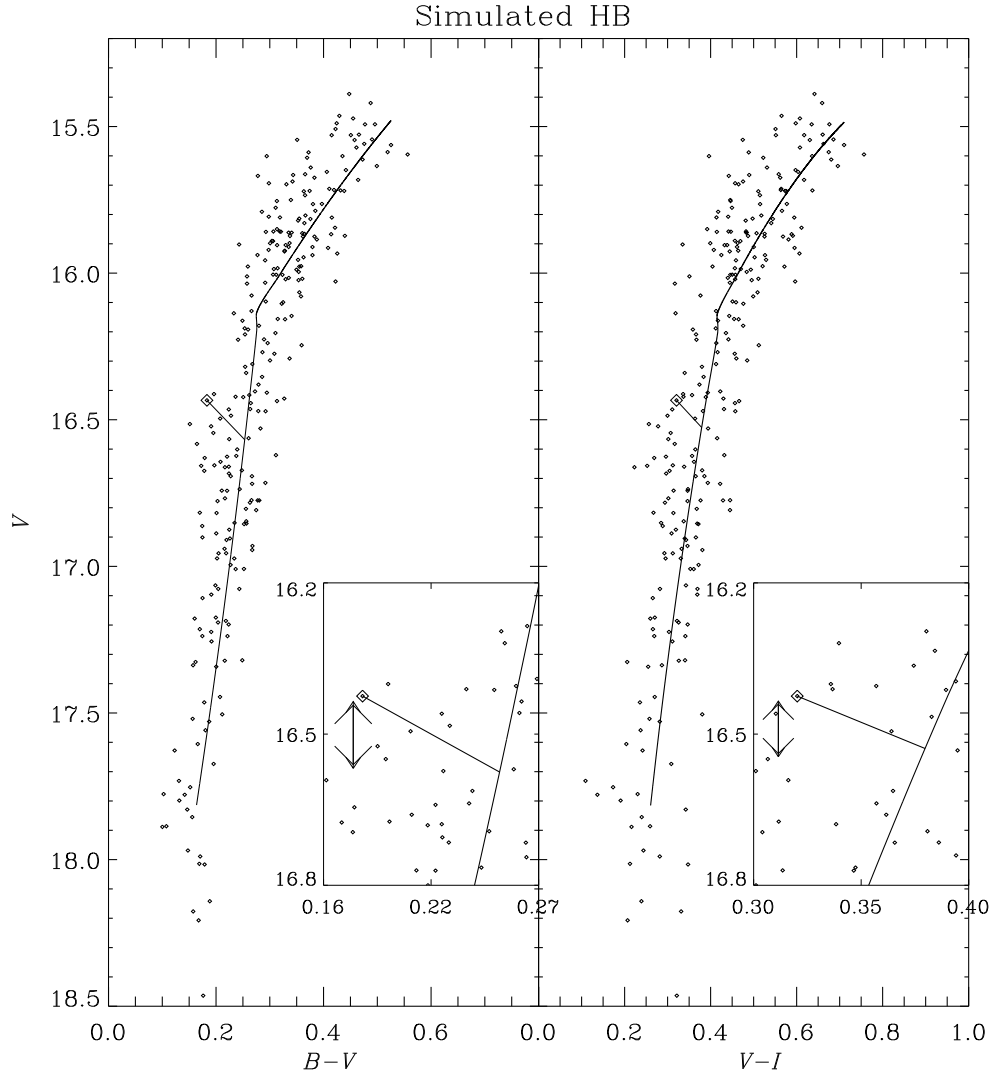


Fig. 6.— Color-magnitude diagrams of a simulated cluster horizontal branch for $B - V$ (left) and $V - I$ (right) color baselines. The simulated data set includes the effects of photometric error and large- and small-scale extinction/reddening variations (§3). The fiducial HB in each panel (solid line) is a fit of two second-order polynomials to stars within the central $r < 2'$ of the simulated cluster (where differential extinction/reddening are relatively small). A sample reddening vector is shown in each panel from a star to the fiducial HB. The region around this vector is magnified in the inset, and an arrow indicates the relative visual extinction $[(\delta A_V)^{BV}$ and $(\delta A_V)^{VI}]$ of the HB star with respect to the fiducial (§4.1.1).

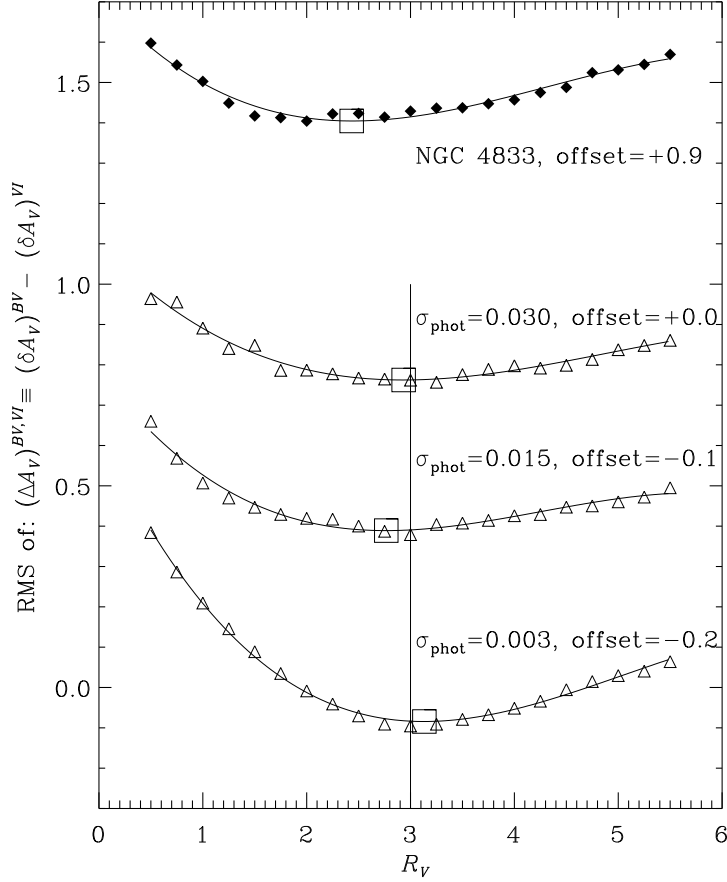


Fig. 7.— Results from the application of the “ A_V RMS” method to NGC 4833 (filled diamonds) and three simulated cluster data sets (open triangles), each with a different level of photometric error. The RMS scatter in $(\Delta A_V)^{BV,VI}$, the difference between relative A_V estimates from the $(B - V, V)$ and $(V - I, V)$ CMDs (see § 4.1), is plotted for a range of test R_V values. The input R_V value used to construct all of these simulations is 3.0 (vertical line). The large open square represents the measured (output) R_V value in each case, marked by the RMS minimum which is interpolated using a polynomial fit (solid curve); the minimum is sharpest for the simulation with the smallest photometric error. Note, the sequences have been offset vertically from one another by the amount indicated for the sake of clarity.

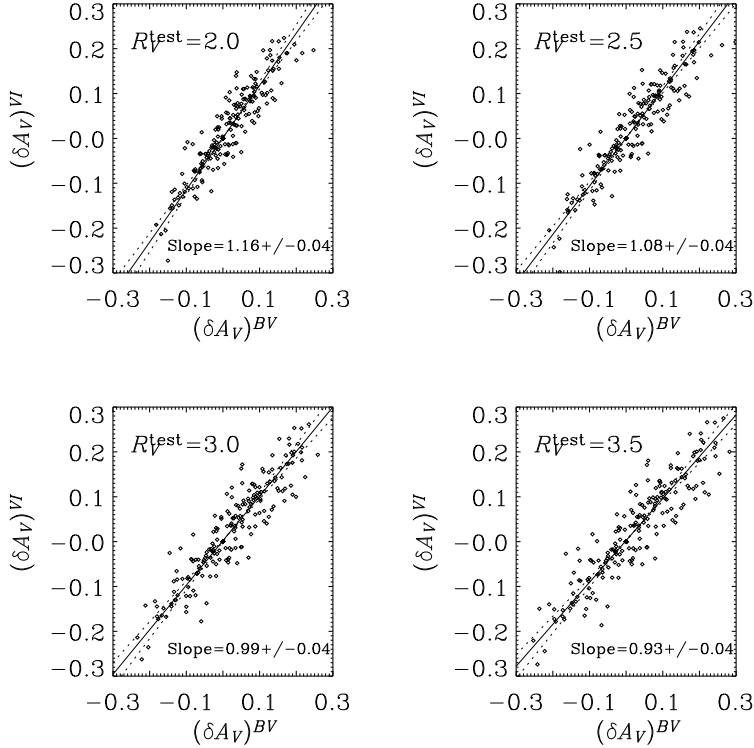


Fig. 8.— Star-by-star comparison of the $(\delta A_V)^{BV}$ and $(\delta A_V)^{VI}$ values measured from the CMDs of a simulated cluster data set designed to mimic the NGC 4833 data set (§ 4.2.1). Each of the four panels assumes a different test R_V value for the purposes of measuring the δA_V parameters. The relationship between the two δA_V measurements tends to be linear. The dashed lines show two linear fits to the data: one uses the x axis as the independent variable and the y axis as the dependent one, and vice versa for the other fit. The solid line represents the mean of these two fits, with the best-fit slope indicated. The slope of the solid line approaches unity when the test R_V equals the input $R_V = 3.0$ used to construct the simulated cluster data set.

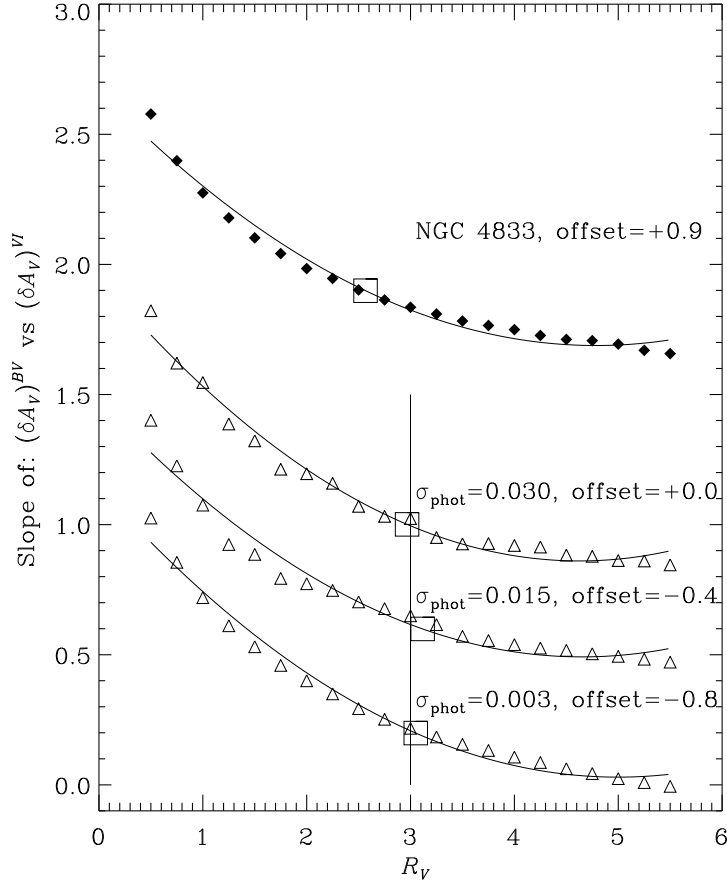


Fig. 9.— Same as Figure 7 for the “ A_V Slope” method (§ 4.2), with the y axis showing the slope of the $(\delta A_V)^{BV}$ versus $(\delta A_V)^{VI}$ relation (solid lines in Fig. 8). A slope of unity, interpolated via a polynomial fit (solid curve), corresponds to the best-fit output R_V value (large open square). The slope vs. test R_V sequence is steepest for the simulation with the smallest photometric error, indicating greatest discriminating power for R_V determination.

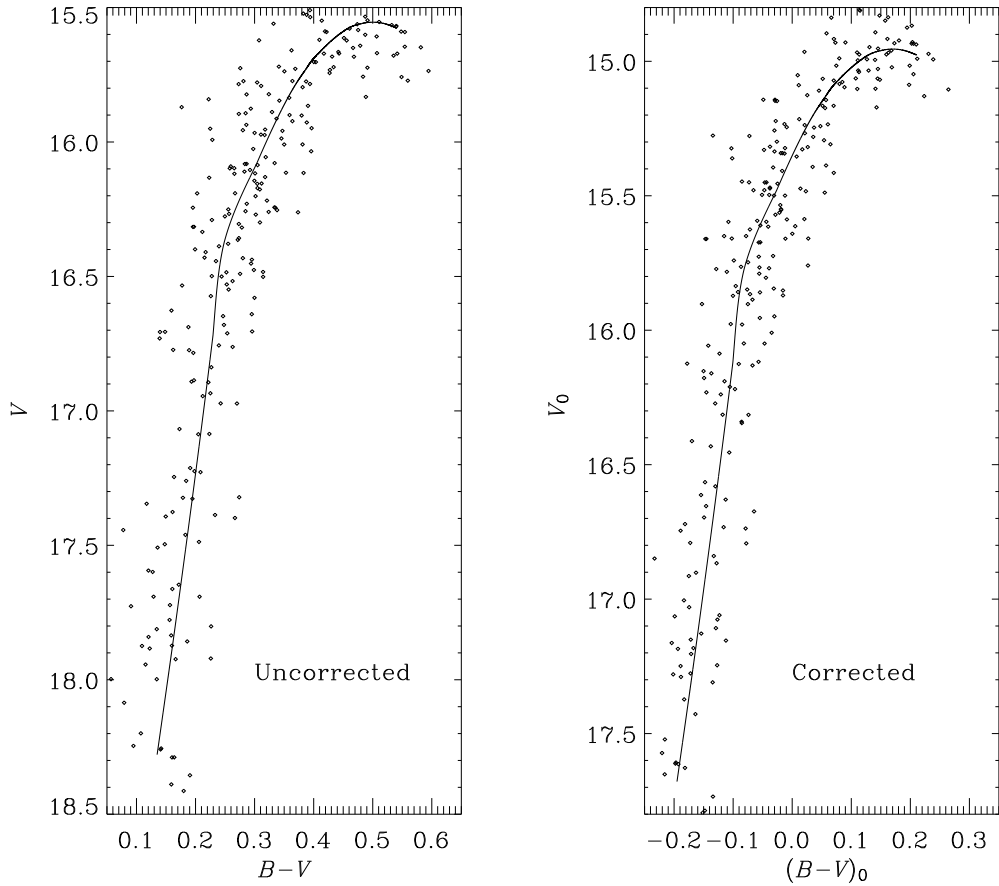


Fig. 10.— (Left) The $(B - V, V)$ color-magnitude diagram of a simulated cluster horizontal branch, including the effects of photometric error and large- and small-scale extinction/reddening variations. (Right) Same, after correcting each star for extinction/reddening using the Schlegel et al. (1998) reddening map. The correction has limited success in tightening the HB because the SFD map cannot resolve small-scale dust variations. The HB fiducial (solid curve) in the right panel is a fit to the corrected data of two second-order polynomials stitched together; the fiducial in the left panel is the same, but with the mean extinction/reddening added to match the uncorrected data.

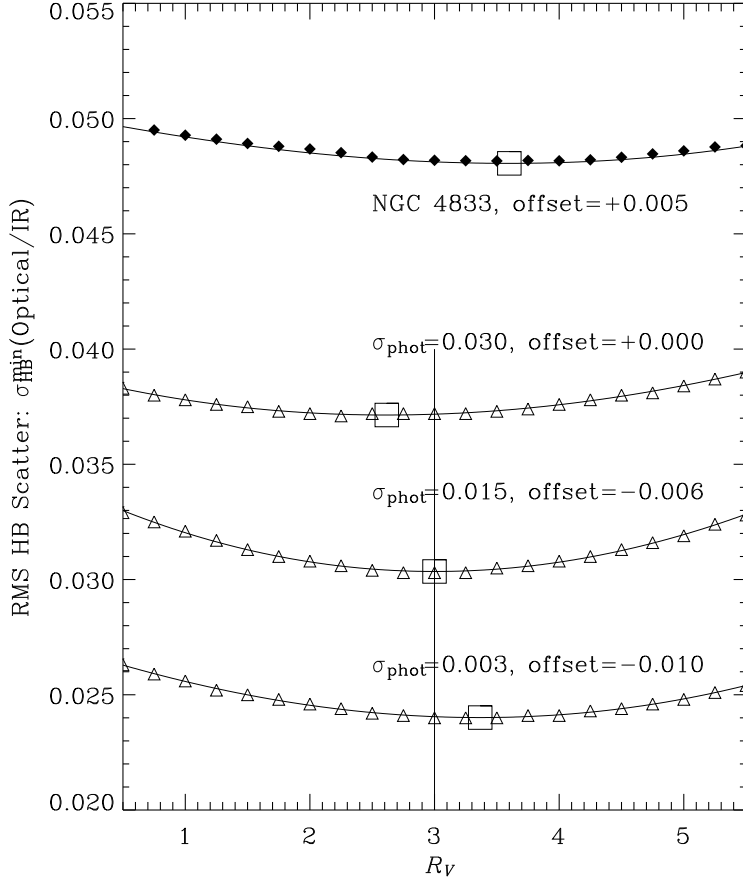


Fig. 11.— Same as Figure 7 for the “Optical/IR” method (§ 4.3), with the y axis showing the RMS scatter of extinction/reddening-corrected HB stars in a $(B - V, V)$ CMD. The scatter is computed based on “shortest distance” from a polynomial fiducial line (see § 3.3). The $E(B - V)$ reddening correction is taken from the Schlegel et al. (1998) dust map; it is converted to A_V using a test R_V value. This method has relatively low discriminating power for R_V determination because the SFD map averages over small-scale reddening variations.

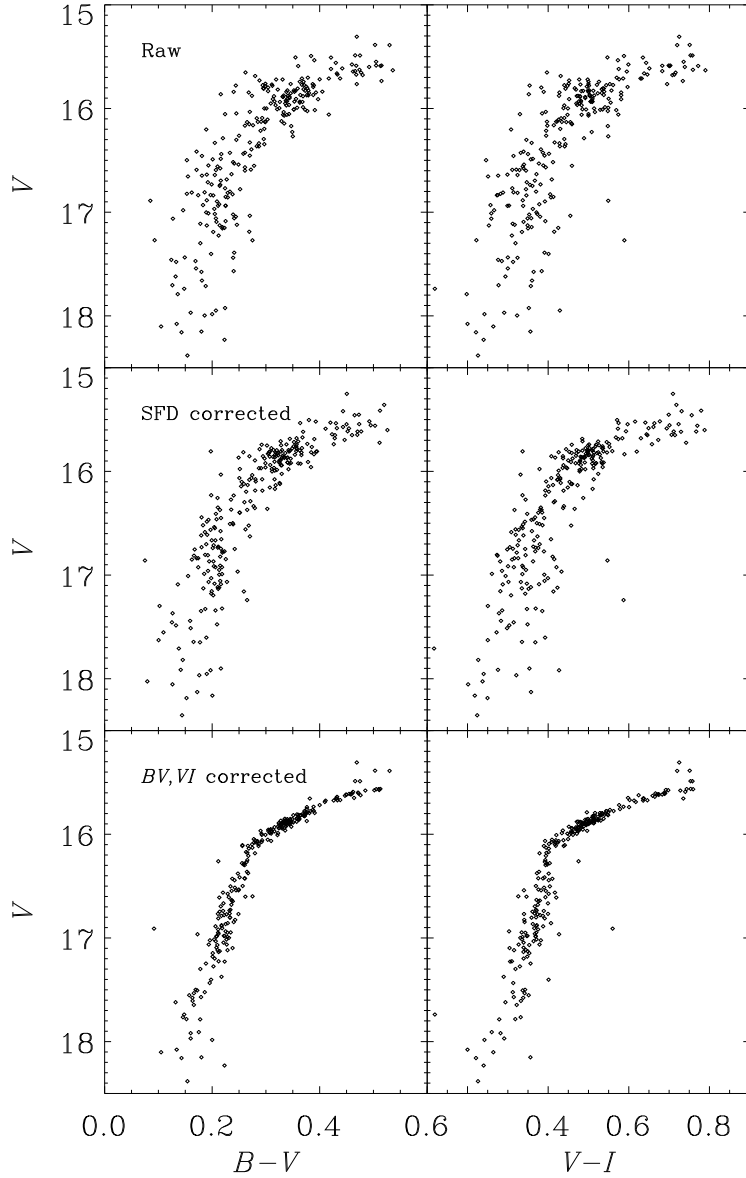


Fig. 12.— Color-magnitude diagrams showing the horizontal branch of NGC 4833 for $B - V$ (left) and $V - I$ (right) color baselines. The top panels show the raw, uncorrected data (same data as in the selection boxes in Fig. 1 and sum of upper and lower panels of Fig. 2). The middle panels show the CMDs after correction for differential extinction/reddening using $E(B - V)$ values from the Schlegel et al. (1998) dust map, scaled to A_V and $E(V - I)$ using the best-fit $R_V = 3.0$ and the corresponding R_I . The mean extinction and reddening are added back to the data to allow direct comparison to the uncorrected data. The data in the bottom panels are corrected for differential visual extinction on a star-by-star basis using the mean of the δA_V values from the $(B - V, V)$ and $(V - I, V)$ CMDs (§ 4.1.1); this is scaled to a color excess using the best-fit R_V and R_I values. The tightness of the resulting HB demonstrates the power of the “ A_V RMS” and “ A_V Slope” methods and the smoothing out of small-scale reddening variations in the SFD dust map (see § 4.4).

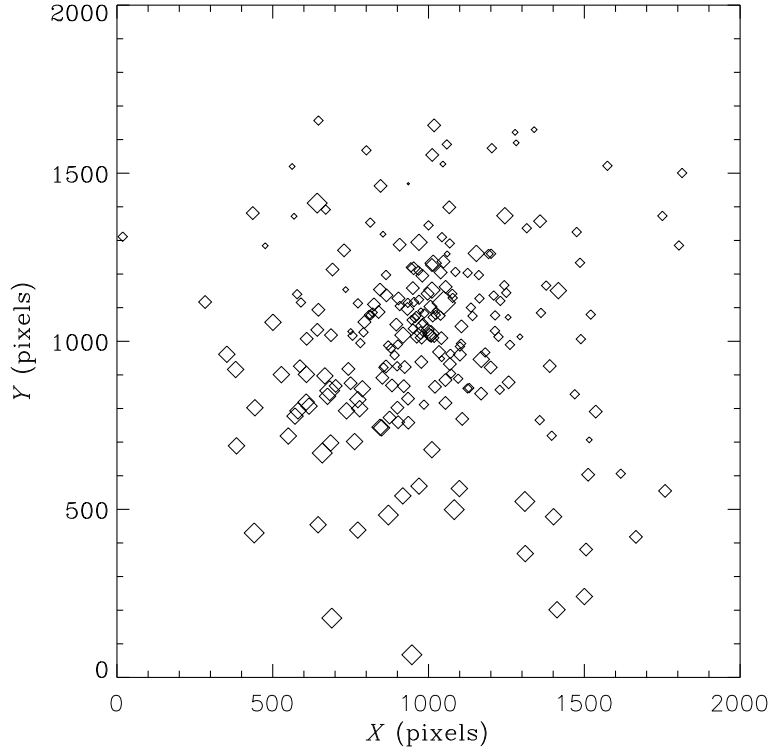


Fig. 13.— A map of the *relative* visual extinction in a $13.5' \times 13.5'$ region of the sky centered on NGC 4833. Each diamond represents the sky position of a cluster HB star. The symbol size scales with $(\delta A_V)^{BV}$ [-0.20 (smallest) to $+0.37$ (largest)], the vertical distance in the CMD between the HB star and the point where the reddening vector drawn from the star intersects the fiducial (§ 4.1.1). The pixel scale for X and Y axes is $0.396'' \text{ pix}^{-1}$. North is along $+Y$ and east is along $+X$.

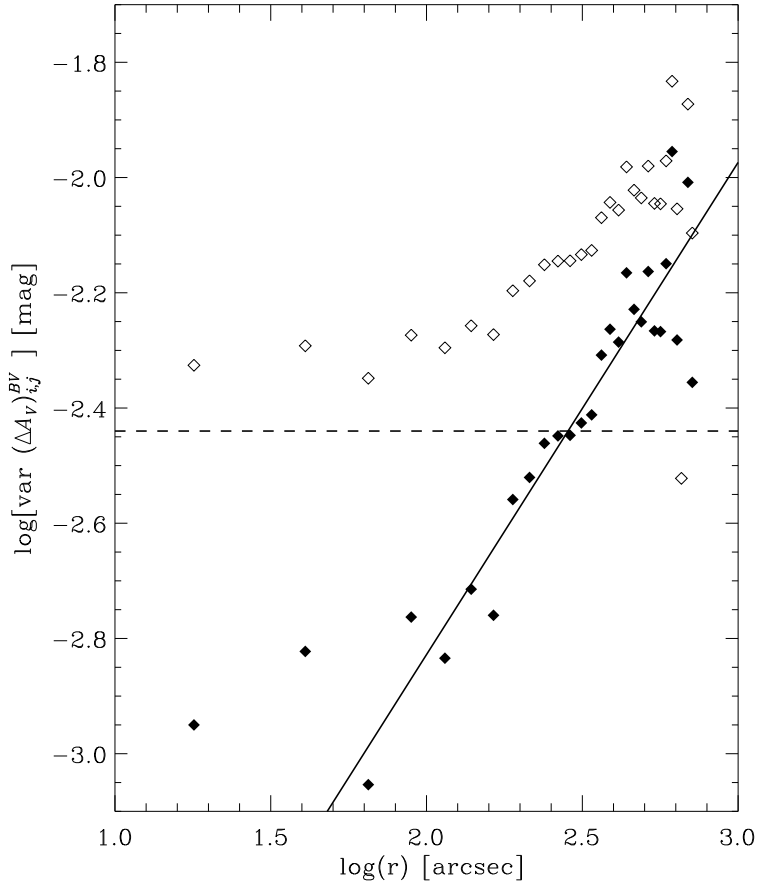


Fig. 14.— The variance of $(\Delta A_V)_{ij}^{BV}$, the difference in relative visual extinction between pairs of NGC 4833 HB stars i and j measured off the $(B - V, V)$ CMD (§4.1.1), as a function of their projected separation r_{ij} (open diamonds). The dashed horizontal line shows the expected amount of variance from photometric errors alone, as derived from the special “ $\sigma_{\text{phot-only}}$ ” simulations that match the mean extinction/reddening and photometric errors in the cluster data set but contain *no* reddening variations (§3.3.1). The filled diamonds show the “variance spectrum” of NGC 4833 after removing the effects of photometric error (§5.1). The solid line power-law fit to the corrected variance spectrum has an index $\beta = +0.9 \pm 0.1$.

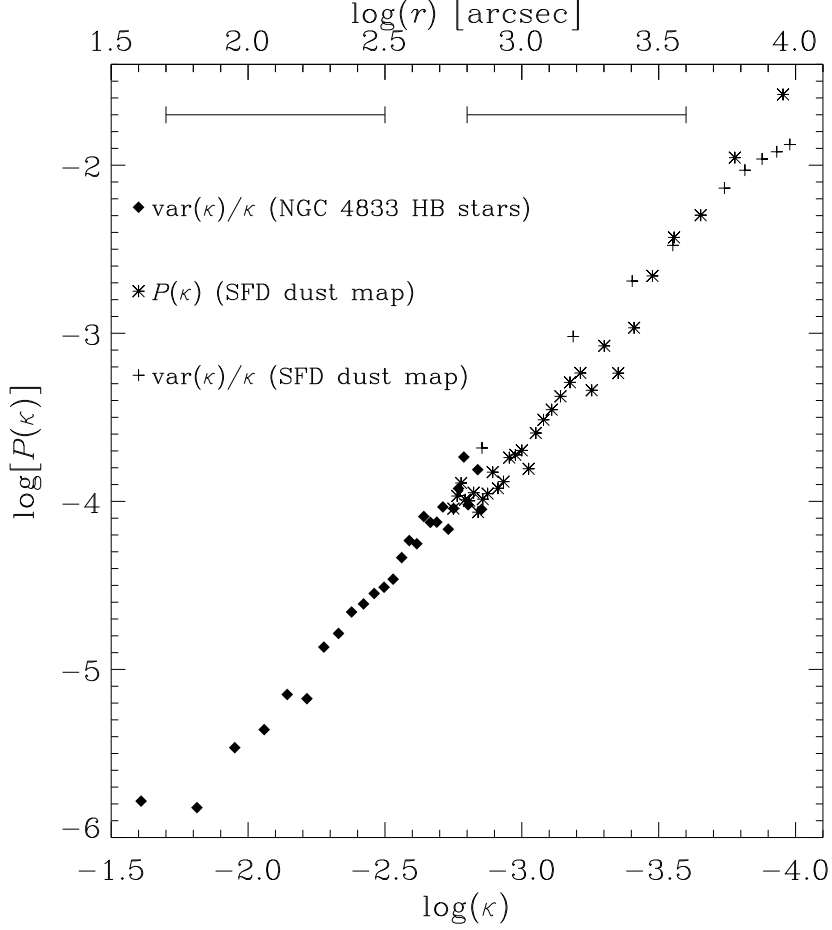


Fig. 15.— The one-dimensional angular power spectrum $P(\kappa)$ of dust in the foreground of NGC 4833, where κ is the reciprocal of the projected separation r . The asterisks are measured from a $10^\circ \times 10^\circ$ Schlegel et al. (1998) reddening map centered on the cluster (§ 5.2). The ‘+’ symbols show $\text{var}(\kappa)/\kappa$ from the SFD map, where the variance of the difference in $E(B - V)^{\text{SFD}}$ between pairs of pixels is calculated for all pixel pairs as a function of their angular separation. Note the general agreement between the SFD $P(\kappa)$ and $\text{var}(\kappa)/\kappa$. The filled diamonds show $\text{var}(\kappa)/\kappa$ (equivalent to the angular power spectrum) derived from the $(B - V, V)$ CMD of NGC 4833 HB stars, corrected for the effects of photometric error (same data as the filled diamonds in Fig. 14 but with a different binning in r). The best-fit power-law indices are: $\alpha = -1.9 \pm 0.1$ over the range $r \sim 1' - 5'$ for optical cluster HB data, and $\alpha = -2.0 \pm 0.1$ over the range $r \sim 10' - 1^\circ$ for the SFD map (radial ranges indicated by horizontal bars near the top).

Table 1. R_V Measurements

Typical Phot. Error (mag)	% of NGC 4833 Phot. Error	True R_V (Input)	Measured R_V (Output) \pm RMS Scatter		
			A_V RMS Method	A_V Slope Method	Optical/IR Method
Monte Carlo Simulations					
0.003	10	2.0	2.05 ± 0.05	1.98 ± 0.04	2.10 ± 0.68
		3.0	3.09 ± 0.09	2.97 ± 0.09	2.88 ± 0.75
		4.0	4.06 ± 0.12	4.29 ± 0.18^a	3.97 ± 0.82
0.015	50	2.0	2.00 ± 0.26	2.04 ± 0.20	1.99 ± 0.64
		3.0	2.97 ± 0.42	3.03 ± 0.45	2.88 ± 0.69
		4.0	3.68 ± 0.50^a	4.13 ± 0.51	3.92 ± 0.81
0.030	100	2.0	2.08 ± 0.68	2.19 ± 0.36^a	1.97 ± 0.57
		3.0	2.60 ± 0.70^a	2.95 ± 0.60	2.89 ± 0.73
		4.0	3.13 ± 0.92^a	3.69 ± 0.79^a	3.87 ± 0.91
NGC 4833					
0.030	—	—	$2.5(\rightarrow 2.9) \pm 0.7^b$	2.6 ± 0.6	3.5 ± 0.7

^aThese cases display a bias in the mean measured (output) R_V (more than ± 0.1) that is significant relative to the error in the mean $[\sigma(R_V)/\sqrt{100}]$.

^bThe measured R_V for NGC 4833 using the “ A_V RMS” method has been corrected upwards by +0.4 to compensate for measurement bias.